

RSC Advances



This is an *Accepted Manuscript*, which has been through the Royal Society of Chemistry peer review process and has been accepted for publication.

Accepted Manuscripts are published online shortly after acceptance, before technical editing, formatting and proof reading. Using this free service, authors can make their results available to the community, in citable form, before we publish the edited article. This *Accepted Manuscript* will be replaced by the edited, formatted and paginated article as soon as this is available.

You can find more information about *Accepted Manuscripts* in the [Information for Authors](#).

Please note that technical editing may introduce minor changes to the text and/or graphics, which may alter content. The journal's standard [Terms & Conditions](#) and the [Ethical guidelines](#) still apply. In no event shall the Royal Society of Chemistry be held responsible for any errors or omissions in this *Accepted Manuscript* or any consequences arising from the use of any information it contains.

Hydrothermal growth of MnO₂/RGO/Ni(OH)₂ on nickel foam with superior supercapacitor performance

Shudi Min^{ab}, Chongjun Zhao^{*a}, Zhuomin Zhang^a, Kun Wang^a, Guorong Chen^a, Xiuzhen Qian^a, Zaiping Guo^{*b}

^a*School of Materials Science and Engineering, East China University of Science and Technology, Shanghai*

200237, P.R. China. Tel: +86-21-6425 0838; Fax: +86-21-6425 0838; E-mail: chongjunzhao@ecust.edu.cn

^b*Institute for Superconducting and Electronic Materials, University of Wollongong, Wollongong, NSW 2522,*

Australia. Tel: 61 2 4221 5731; Fax: 61 2 4221 5731; E-mail: zguo@uow.edu.au

Abstract

A MnO₂/reduced graphene oxide (RGO)/Ni(OH)₂ composite with arrays of mushroom-headed needle-like nanostructures on its top surface was designed and directly grown on nickel foam through a one-pot hydrothermal process without the addition of any source of extra Ni ions. Based on the redox reaction of elemental Ni and graphene oxide (GO), along with electrostatic forces between Mn ions from the solution and GO, there was good contact and strong interaction between the different components, as well as between the active materials and the Ni substrate. Hence, the as-synthesized MnO₂/RGO/Ni(OH)₂ composite can be utilized as supercapacitor electrode with a high areal mass loading of 5.4 mg cm⁻². It exhibits superior performance: 17.8 F cm⁻² (i.e., 3296.9 F g⁻¹) at 7 mA cm⁻² (1.3 A g⁻¹), as well as capacity retention of 90.2%, even after 5,000 cycles at 20 mA cm⁻² (3.7 A g⁻¹).

Keywords: Manganese dioxide/Reduced graphene oxide/Nickel hydroxide, Binder-free, Mushroom-headed needle-like, Hydrothermal process, Supercapacitor

1. Introduction

Supercapacitors have attracted great attention for energy storage because of their high power density, long cycle lifetime, and high reliability [1, 2]. In particular, pseudocapacitive materials such as metal oxides/hydroxides have attracted a great deal of interest due to their high specific capacitances and energy densities [3, 4]. Among these materials, Ni(OH)₂ is one of the most promising candidates because of its low-cost, environmentally-friendly nature, and its high redox activity [5, 6]. Nevertheless, some challenges are still obstructing its application, and one of the major drawbacks for pure Ni(OH)₂ is its very low electrical conductivity ($\sim 10^{-17}$ S cm⁻¹) [7], which is a barrier to the application of Ni(OH)₂ as an electrode material.

In order to overcome this problem, designing and developing a Ni(OH)₂-based composite is an important approach. One route is to combine Ni(OH)₂ with carbon materials, especially nano-carbon materials, e.g., carbon nanotubes or graphene, which will improve the electronic conductivity and thus facilitate good electrochemical performance of the Ni(OH)₂ [8-10]. Alternatively, a second strategy is to integrate Ni(OH)₂ with another metal oxide/hydroxide. Due to the synergistic effects of the individual components, composites of metal oxides (hydroxides) with Ni(OH)₂ have delivered good performances [11-13]. Considering the metal oxides, MnO₂ is a typical supercapacitor electrode material due to its particular advantages, which include low cost, low toxicity, high theoretical capacity, and stable structure. Recently, composites of MnO₂/Ni(OH)₂ were fabricated and used as good electrode material for supercapacitors [14-16]. Furthermore, a new hybrid composite

[Ni(OH)₂/MnO₂/RGO] was prepared by introducing an RGO component [17]. Despite all of the above achievements, there are still some challenges for MnO₂/Ni(OH)₂-based composite electrode materials, e.g., there have been no more reports on MnO₂/Ni(OH)₂/RGO, and the comprehensive electrochemical performance in terms of both specific capacitance and cycle life of these MnO₂/Ni(OH)₂ composites can be further improved.

Besides the electrode composition, the structure also strongly affects the electrochemical performance of supercapacitor electrodes. It is necessary to build a stable, porous, and nanosized structure with good electronic contact between the individual components, which is usually accomplished during the synthesis process. Moreover, from the viewpoint of synthesis, it is necessary to design and develop a simple and facile method.

Recently, we found that graphene oxide (GO) could be reduced and made to cover a nickel foam (NF) substrate, while the surface metal at the top of the substrate was oxidized and transformed in-situ into Ni(OH)₂, and thus RGO/Ni(OH)₂/NF was formed [18]. At the same time, MnO₂ can be anchored on the upper surface of the RGO, based on the electrostatic interaction between the Mn ions and the GO by introducing Mn salt into the solution. These indicate that a new method can be designed and developed to synthesize a binder-free MnO₂/RGO/Ni(OH)₂/NF composite electrode, which, to the best of our knowledge, has not been previously reported. This architecture of MnO₂/RGO/Ni(OH)₂ gives both the Ni(OH)₂ and the MnO₂ good contact with the highly conductive RGO, and then with the current

collector (nickel foam), which enhances the electrochemical capacitance of the composite. In addition, the presence of soft RGO buffers the volume changes during the repeated charging/discharging, which promotes the cyclability of the MnO₂/RGO/Ni(OH)₂ composite.

Herein, we have synthesized MnO₂/RGO/Ni(OH)₂ composite film on nickel foam through a simple one-step hydrothermal process [see the Electronic Supplementary Information (ESI) for more experimental details]. The nanostructure, consisting of mushroom-headed needle-like MnO₂ arrays standing vertically on RGO-covered Ni(OH)₂ layers was formed *in-situ* along with the intervening layers on the nickel foam surface. The as-prepared MnO₂/RGO/Ni(OH)₂ composite film was directly utilized as a binder-free supercapacitor electrode, which showed superior performance of 17.8 F cm⁻² (i.e., 3296.9 F g⁻¹) at 7 mA cm⁻² and a capacity retention of 90.2% (5,000 cycles).

2. Results and discussion

The XRD patterns of MnO₂/RGO/Ni(OH)₂/NF (MRNN) and RGO/Ni(OH)₂/NF (RNN) are shown in Fig. 1(a) and Fig. S1. Three peaks centered at 44.6°, 51.9°, and 76.4°, assigned to the (111), (200), and (220) planes of metallic nickel (JCPDS No. 01-1258), respectively [19], are clearly observed in all patterns. The diffraction peaks at 19.3°, 33.2°, 38.6°, 52.0°, 59.1°, 62.7°, 70.4°, and 72.6° in the RNN and MRNN composites can be ascribed to the (001), (100), (101), (102), (110), (111), (103), and (201) crystalline planes of β-phase Ni(OH)₂ (JCPDS No. 14-0117), respectively [14,

15]. Besides, a weak signal of γ - MnO_2 (JCPDS No. 14-0644) is observed at 22.4° , 34.5° , and 38.7° in the MRNN composite, which corresponds to the (120), (031), and (230) planes [13, 17]. These indicate that the surface of the Ni foam was well decorated with the $\text{Ni}(\text{OH})_2$ and MnO_2 in the presence of GO.

XPS was also performed to further identify the chemical composition at the region of 0-1100 eV [Fig. 1(b-d)]. The survey spectrum of the MRNN composite mainly shows carbon (C 1s), oxygen (O 1s), manganese, and nickel species [Fig. 1(b)]. The Ni 2p XPS spectrum [Fig. 1(c)] shows two main peaks at 872.8 and 855.2 eV, which are assigned to Ni $2p_{1/2}$ and Ni $2p_{3/2}$, respectively, with a spin-energy separation of 17.6 eV. Besides, the satellite peaks (satellite of Ni $2p_{1/2}$: 878.8 eV; satellite of Ni $2p_{3/2}$: 860.8 eV) are also observed, which are in accordance with previously reported data [6, 20-22]. The XPS spectra on carbon, oxygen and Ni for MRNN composite are well consistent with those for RNN composite, in which GO is well transformed into RGO [18]. In addition, the Mn 2p XPS spectrum [Fig. 1(d)] displays two characteristic peaks at 654 and 642.4 eV, corresponding to Mn $2p_{1/2}$ and Mn $2p_{3/2}$, respectively, with a spin-energy separation of 11.6 eV, which are associated with the MnO_2 phase previously reported [15, 23, 24]. These XPS results confirm the presence of $\text{Ni}(\text{OH})_2$ and MnO_2 in the MRNN composite.

Fig. 2(a-d) presents FESEM images of the $\text{MnO}_2/\text{Ni}(\text{OH})_2/\text{NF}$ (MNN), $\text{RGO}/\text{Ni}(\text{OH})_2/\text{NF}$ (RNN), and MRNN composites. In contrast to the $\text{Ni}(\text{OH})_2/\text{NF}$ sample synthesized with NF and H_2O [18], the surface of the $\text{MnO}_2/\text{Ni}(\text{OH})_2/\text{NF}$ composite [Fig. 2(a)] is mainly covered by random and uneven MnO_2 wires deposited

from solution, while the RGO/Ni(OH)₂/NF composite consists of mackerel-scale Ni(OH)₂ flakes on the NF base and a corrugated graphene coating [Fig. 2(b)]. The RGO sheets are uniformly distributed on the surface of the Ni(OH)₂ layer [18, 25], providing a large surface area for depositing the MnO₂ coming from the solution. The cross-sectional SEM image of the MRNN composite in Fig. 2(c) shows that the nanostructured MnO₂ arrays line up, with the array elements having the shape of mushroom-headed needles. The highly magnified SEM [Fig. 2(d)] and top-view SEM images [Fig. S2(a) in the ESI] show that numerous MnO₂ nanoparticles have grown into mushroom-headed needle-like MnO₂ nanostructures, and stand in vertical arrays on the RGO-covered Ni(OH)₂ layers that were formed *in-situ* on the NF surface. It is thus apparent that the presence of GO significantly affects the arrangement of the MnO₂ nanostructure and facilitates the formation of ordered oriented array structures in the composite films on Ni foam substrate [18, 26]. Fig. S2(b)-(e) presents the corresponding energy dispersive spectroscopy (EDS) elemental maps of carbon [Fig. S2(b)], oxygen [Fig. S2(c)], nickel [Fig. S2(d)], and manganese [Fig. S2(e)] in the MRNN composite, and they indicate the diverse structure of the MnO₂/RGO/Ni(OH)₂ film uniformly coated on the NF surface. The EDS spectrum of the MRNN composite (Fig. S3) also shows that the composite mainly contains the elements Ni, Mn, O, and C, which should be attributed to the component of Ni(OH)₂, MnO₂, and RGO. These results are well accordance with the XRD and XPS analysis.

A TEM image of MnO₂ nanowires with diameter of about 50 nm is shown in Fig. 2(e), and the corresponding high resolution TEM (HRTEM) image in Fig. 2(f)

exhibits that the calculated lattice spacing is about 0.27 nm, which is accordance with the (031) planes of γ -MnO₂, confirming its crystalline nature in consistent with the XRD results.

We propose a possible formation mechanism to the MRNN composite based on the experimental results and some earlier work [18, 25, 27], are illustrated in Scheme 1. During the hydrothermal process, the Ni at the top of the foam is directly oxidized into Ni(OH)₂, and GO is reduced to RGO, which successfully covers the surface of the Ni(OH)₂ layer. Furthermore, in this work, an array of MnO₂ nanostructures, deposited from Mn²⁺ in the solution, is vertically packed on the top side of the RGO at the same time, eventually forming a multilayer diverse structure: MnO₂/RGO/Ni(OH)₂ film on Ni foam substrate. Due to the electrostatic effect, the negatively charged GO attracts the positively charged Mn²⁺, which facilitates uniform anchoring of the MnO₂ array on the GO nanosheets of this three-dimensional (3D) diverse structure [28, 29]. The low magnification FESEM images of RGO/Ni(OH)₂/NF and MnO₂/RGO/Ni(OH)₂/NF [Fig. S4(a) and (b)] also indicate the difference in the NF surface.

The performance of the MRNN composite films as electrode materials in supercapacitors was evaluated using cyclic voltammetry (CV) and galvanostatic charge/discharge (GCD). Fig. 3(a) shows the CV curves of the MRNN electrode in 1 M KOH aqueous electrolyte at various scan rates ranging from 1 to 10 mV s⁻¹. A pair of redox peaks within the range of -0.1-0.5 V [vs. saturated calomel electrode (SCE)] can be mainly ascribed to a faradaic redox reaction related to Ni(OH)₂/NiOOH [18],

suggesting that the specific capacitance of the MRNN composite is primarily attributable to pseudocapacitive capacitance, based on the redox mechanism [17, 26]. As shown in Fig. S5, the contribution of Ni foam to the capacitance of MRNN composite electrode can be negligible [12, 16].

Fig. 3(b-d) shows the GCD performance of the MRNN composite. The specific capacitance C_s can be calculated from the equation (2) [in the ESI] [30]. Fig. 3(b) shows the GCD curves at various current densities of 7, 8, 9, 10, 11, 12, 13, 14, 15, and 20 mA cm⁻² (corresponding to 1.30, 1.48, 1.67, 1.85, 2.04, 2.22, 2.41, 2.60, 2.78, and 3.70 F g⁻¹, respectively), over the potential window from -0.1 V to 0.5 V for the MRNN electrode. The areal capacitance and gravimetric capacitance values of the MRNN electrode can be calculated and plotted in Fig. 3(c). The highest areal capacitance achieved on the MRNN electrode is 17.8 F cm⁻² (i.e., 3296.9 F g⁻¹) at 7 mA cm⁻², which is much higher than those of the related works [31-33]. In addition, compared with the preparation methods in these three references, the unique merit in our work is that Ni foam was used as not inert but active substrate, i.e., Ni was *in situ* converted into Ni(OH)₂ through the redox reaction with GO, which supplied a good support for the subsequent deposition of MnO₂. It is worth noting that RGO play a key role in contacting both lower Ni(OH)₂ layer and upper MnO₂ layer.

The composite electrode retains an areal capacitance of over 8 F cm⁻², even at the current density of 20 mA cm⁻² [Fig. 3(c)]. The vertically aligned nanostructured MnO₂ makes it possible to expose almost all the surface, providing plentiful electroactive sites for redox reactions [34].

The long-term cycling performance of this composite electrode was recorded, as shown in Fig. 3(d). It can be observed that the specific capacitance increases by about 1.5% during the first 500 cycles, which may be due to electrode activation, which increases the number of available active sites and allows the trapped ions to gradually diffuse out [30, 34]. Importantly, the MRNN composite electrode exhibits superior cycling stability, with a stable capacitance (only 9.8% capacity decay) after 5,000 cycles of charging and discharging at a current density of 20 mA cm^{-2} , and furthermore, it has 88% capacity retention, even after 6,000 cycles of charging and discharging. The superior cycling performance is related to its unique stable structure of the MRNN composite, and the comparison of FESEM images [Fig. S6 and Fig. 2(d)] before and after charged and discharged for 5000 cycles prove that the morphology of MRNN was well kept. The volume changes of the active materials during the redox reactions are the main cause of limited cycle life [2]. The structure of RGO/Ni(OH)₂, it is worth noting, even without upper nanostructured MnO₂ array, also contributes to the cycling stability by reducing the shock of volume changes, based on both the soft and highly flexible RGO and the uneven rather than flat Ni(OH)₂ surface [25].

3. Conclusion

In summary, MnO₂ was introduced into RGO/Ni(OH)₂ (MnO₂/RGO/Ni(OH)₂) through a facile one-step hydrothermal approach. This composite electrode exhibits a superior specific capacitance up to 17.8 F cm^{-2} (i.e., 3296.9 F g^{-1}) at a current density

of 7 mA cm^{-2} (1.3 A g^{-1}) in 1 M KOH solution. In addition, the electrode exhibits excellent cycling stability, with capacity retention of 90.2% after 5,000 cycles (vs. 92.5% after 1,000 cycles for $\text{Ni(OH)}_2/\text{RGO}$), indicating that it has a promising application as an efficient electrode for high-performance supercapacitors.

Acknowledgements: We are grateful for the support of the National Natural Science Foundation of China (No. 20504026), the Shanghai Natural Science Foundation (No. 13ZR1411900), the Shanghai Leading Academic Discipline Project (B502), the Shanghai Key Laboratory Project (08DZ2230500), the Australian Research Council (ARC) through an ARC Discovery project (DP1094261), and the China Scholarship Council. The authors would like to thank Dr. T. Silver for critical reading of the manuscript.

References

- [1] P. Simon and Y. Gogotsi, *Nat. Mater.*, 2008, **7**, 845-854.
- [2] J.R. Miller and P. Simon, *Science*, 2008, **321**, 651-652.
- [3] F. Ataherian and N.L. Wu, *Electrochem. Commun.*, 2011, **13**, 1264-1267.
- [4] G.X. Pan, X.H. Xia, F. Cao, P.S. Tang and H.F. Chen, *Electrochem. Commun.*, 2013, **34**, 146-149.
- [5] Z. Tang, C.H. Tang and H. Gong, *Adv. Funct. Mater.*, 2012, **22**, 1272-1278.
- [6] F.Q. Zhang, D. Zhu, X. Chen, X. Xu, Z. Yang, C. Zou, K.Q. Yang and S.M. Huang, *Phys. Chem. Chem. Phys.*, 2014, **16**, 4186-4192.
- [7] Z.P. Sun and X.M. Lu, *Ind. Eng. Chem. Res.*, 2012, **51**, 9973-9979.
- [8] H.J. Yan, J.W. Bai, J. Wang, X.Y. Zhang, B. Wang, Q. Liu and L.H. Liu, *CrystEngComm*, 2013, **15**, 10007-10015.
- [9] L.L. Zhang, Z.G. Xiong and X.S. Zhao, *J. Power Sources*, 2013, **222**, 326-332.
- [10] Y.F. Liu, G.H. Yuan, Z.H. Jiang, Z.P. Yao and M. Yue, *J. Alloys Compd.*, 2015, **618**, 37-43.
- [11] H. Jiang, C.Z. Li, T. Sun and J. Ma, *Chem. Commun.*, 2012, **48**, 2606-2608.
- [12] C.H. Tang, X.S. Yin and H. Gong, *ACS Appl. Mater. Interfaces*, 2013, **5**, 10574-10582.
- [13] H. Chen, L.F. Hu, Y. Yan, R.C. Che, M. Chen and L.M. Wu, *Adv. Energy Mater.*, 2013, **3**, 1636-1646.
- [14] M. Kundu and L.F. Liu, *J. Power Sources*, 2013, **243**, 676-681.
- [15] M. Huang, Y.X. Zhang, F. Li, L.L. Zhang, Z.Y. Wen and Q. Liu, *J. Power*

- Sources*, 2014, **252**, 98-106.
- [16] T. Zhai, F.X. Wang, M.H. Yu, S.L. Xie, C.L. Liang, C. Li, F.M. Xiao, R.H. Tang, Q.X. Wu, X.H. Lu and Y.X. Tong, *Nanoscale*, 2013, **5**, 6790-6796.
- [17] H. Chen, S.X. Zhou and L.M. Wu, *ACS Appl. Mater. Interfaces*, 2014, **6**, 8621-8630.
- [18] S.D. Min, C.J. Zhao, G.R. Chen and X.Z. Qian, *Electrochim. Acta*, 2014, **115**, 155-164.
- [19] S.D. Min, C.J. Zhao, G.R. Chen, Z.M. Zhang and X.Z. Qian, *Electrochim. Acta*, 2014, **135**, 336-344.
- [20] L. Jiang, R.J. Zou, W.Y. Li, J.Q. Sun, X.H. Hu, Y.F. Xue, G.J. He and J.Q. Hu, *J. Mater. Chem. A*, 2013, **1**, 478-481.
- [21] Z. Wu, X.L. Huang, Z.L. Wang, J.J. Xu, H.G. Wang and X.B. Zhang, *Sci. Rep.*, 2014, **4**, 3669.
- [22] J. Yan, Z.J. Fan, W. Sun, G.Q. Ning, T. Wei, Q. Zhang, R.F. Zhang, L.J. Zhi and F. Wei, *Adv. Funct. Mater.*, 2012, **22**, 2632-2641.
- [23] J.P. Liu, J. Jiang, M. Bosman and H.J. Fan, *J. Mater. Chem.*, 2012, **22**, 2419-2426.
- [24] G.Y. Zhu, Z. He, J. Chen, J. Zhao, X.M. Feng, Y.W. Ma, Q.L. Fan, L.H. Wang and W. Huang, *Nanoscale*, 2014, **6**, 1079-1085.
- [25] S.D. Min, C.J. Zhao, Z.M. Zhang, G.R. Chen, X.Z. Qian and Z.P. Guo, *J. Mater. Chem. A*, 2015, **3**, 3641-3650.

- [26] H.L. Wang, H.S. Casalongue, Y.Y. Liang and H.J. Dai, *J. Am. Chem. Soc.*, 2010, **132**, 7472-7477.
- [27] C.J. Zhao, S.L. Chou, Y.X. Wang, C.F. Zhou, H.K. Liu and S.X. Dou, *RSC Adv.*, 2013, **3**, 16597-16603.
- [28] L.Q. Wang, X.C. Li, T.M. Guo, X.B. Yan and B.K. Tay, *Int. J. Hydrogen Energy*, 2014, **39**, 7876-7884.
- [29] J.T. Zhang, S. Liu, G.L. Pan, G.R. Li and X.P. Gao, *J. Mater. Chem. A*, 2014, **2**, 1524-1529.
- [30] C.Z. Yuan, J.Y. Li, L.R. Hou, X.G. Zhang, L.F. Shen and X.W. Lou, *Adv. Funct. Mater.*, 2012, **22**, 4592-4597.
- [31] M.J. Pang, G.H. Long, S. Jiang, Y. Ji, W. Han, B. Wang, X.L. Liu, and Y.L. Xi, *Electrochim. Acta*, 2015, **161**, 297-304.
- [32] A. Bello, O.O. Fashedemi, M. Fabiane, J.N. Lekitima, K.I. Ozoemena, and N. Manyala, *Electrochim. Acta*, 2013, **114**, 48-53.
- [33] Y.Q. Zhao, D.D. Zhao, P.Y. Tang, Y.M. Wang, C.L. Xu, and H.L. Li, *Mater. Lett.*, 2012, **76**, 127-130.
- [34] X.J. Zhang, W.H. Shi, J.X. Zhu, W.Y. Zhao, J. Ma, S. Mhaisalkar, T.L. Maria, Y.H. Yang, H. Zhang, H.H. Hng and Q.Y. Yan, *Nano Res.*, 2010, **3**, 643-652.

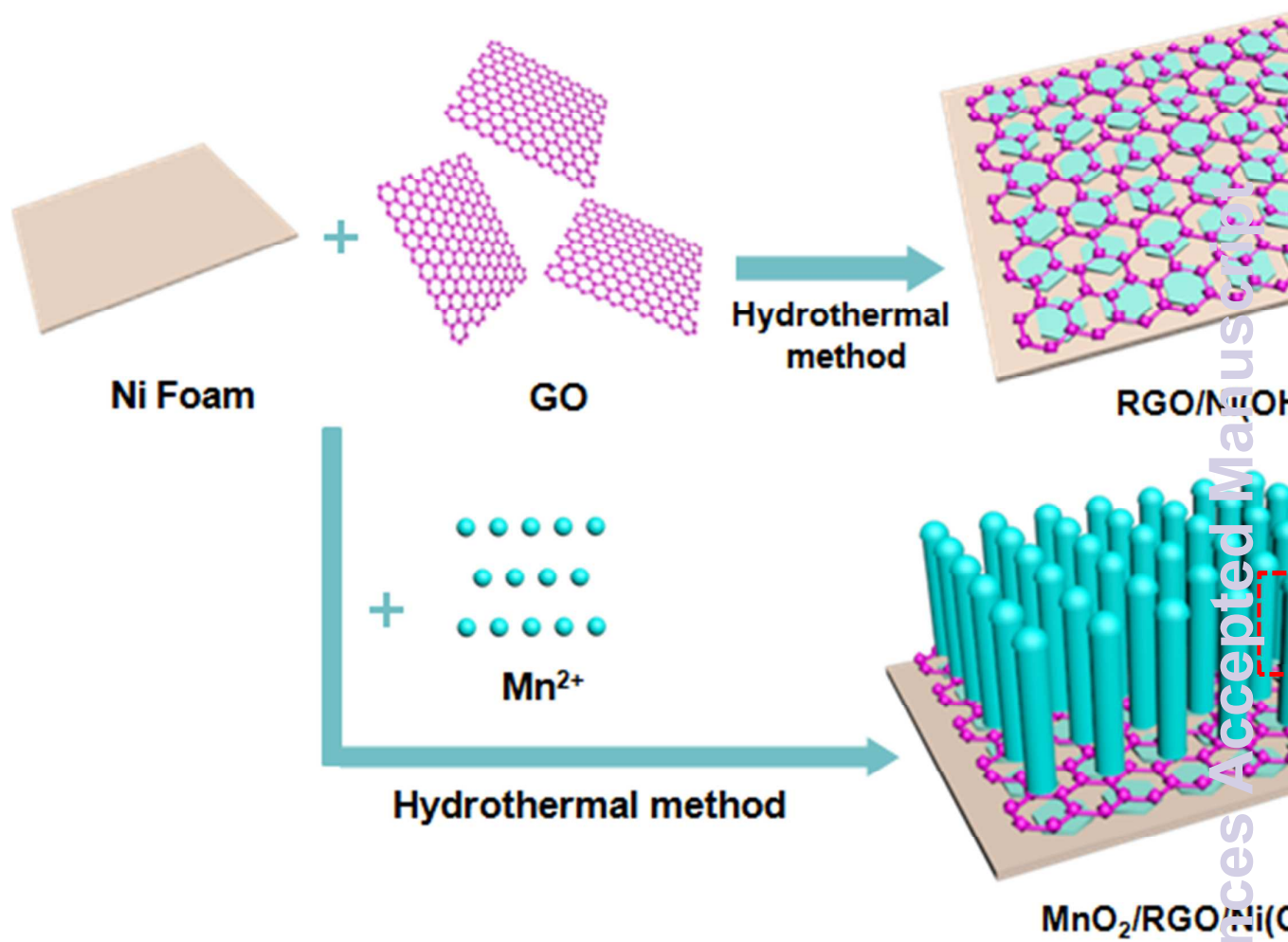
Figure Captions

Fig. 1. (a) XRD pattern of $\text{MnO}_2/\text{RGO}/\text{Ni}(\text{OH})_2/\text{NF}$ (MRNN) composite; (b)-(d) XPS spectra of MRNN composite: (b) survey spectrum (A in brackets denotes Auger electron peaks), (c) Ni 2p spectrum, and (d) Mn 2p spectrum of the MRNN composite.

Fig. 2. FESEM images of (a) $\text{MnO}_2/\text{Ni}(\text{OH})_2/\text{NF}$ (MNN) composite, (b) $\text{RGO}/\text{Ni}(\text{OH})_2/\text{NF}$ (RNN) composite, (c-d) $\text{MnO}_2/\text{RGO}/\text{Ni}(\text{OH})_2/\text{NF}$ (MRNN) composite. (e) TEM and (f) HRTEM images of MnO_2 in MRNN composite.

Fig. 3. (a) Cyclic voltammograms (CV) of MRNN electrode at various scan rates (1, 2, 5, and 10 mV s^{-1}); (b) galvanostatic charge/discharge (GCD) curves of MRNN electrode at various current densities; (c) current density dependence of the areal capacitance (lower curve) and the specific capacitance (upper curve) of the MRNN electrode; and (d) cycling performance of the MRNN electrode at a current density of 20 mA cm^{-2} .

Scheme 1. Schematic representation of the formation processes of the $\text{RGO}/\text{Ni}(\text{OH})_2/\text{NF}$ (RNN) and $\text{MnO}_2/\text{RGO}/\text{Ni}(\text{OH})_2/\text{NF}$ (MRNN) composites.



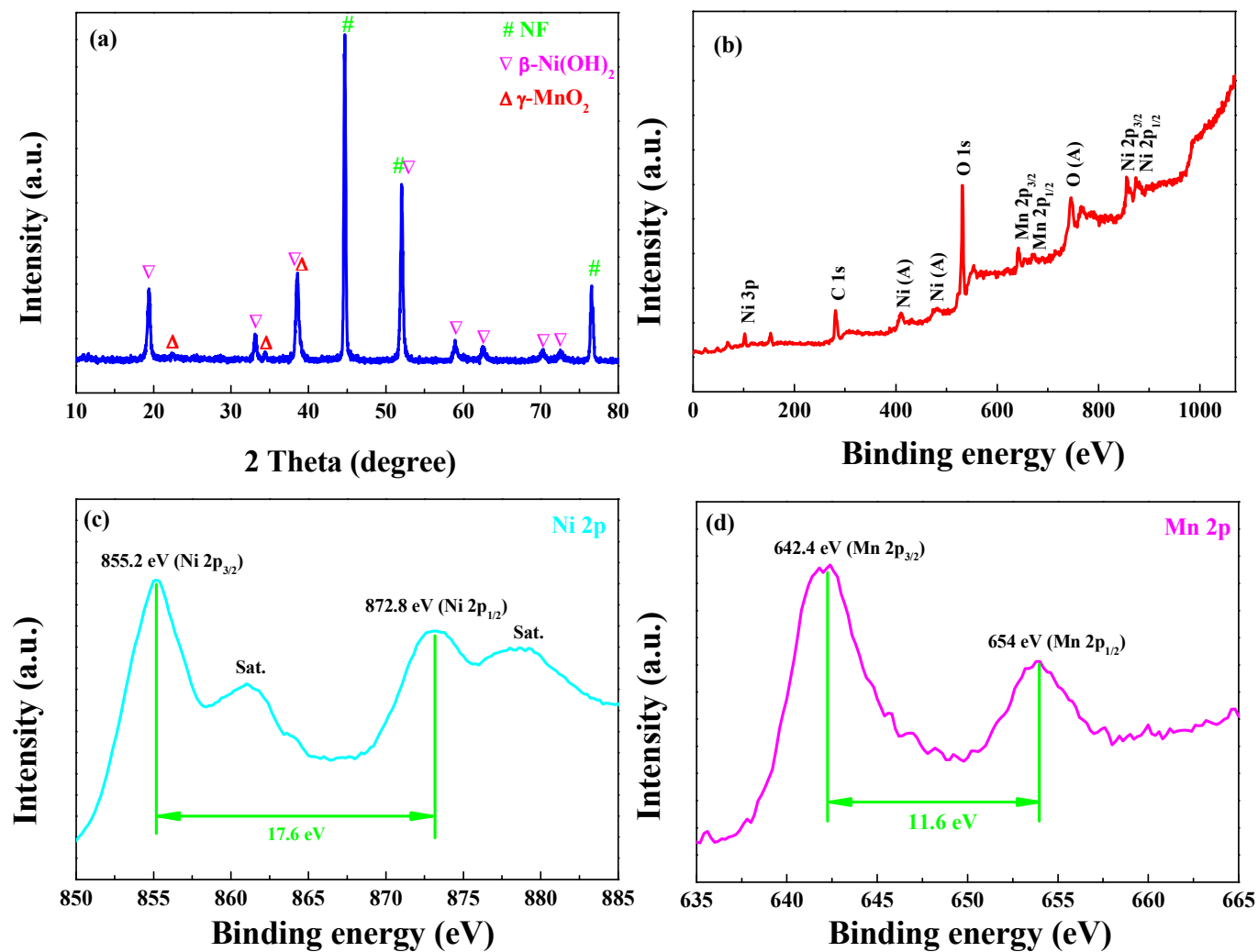


Fig. 1

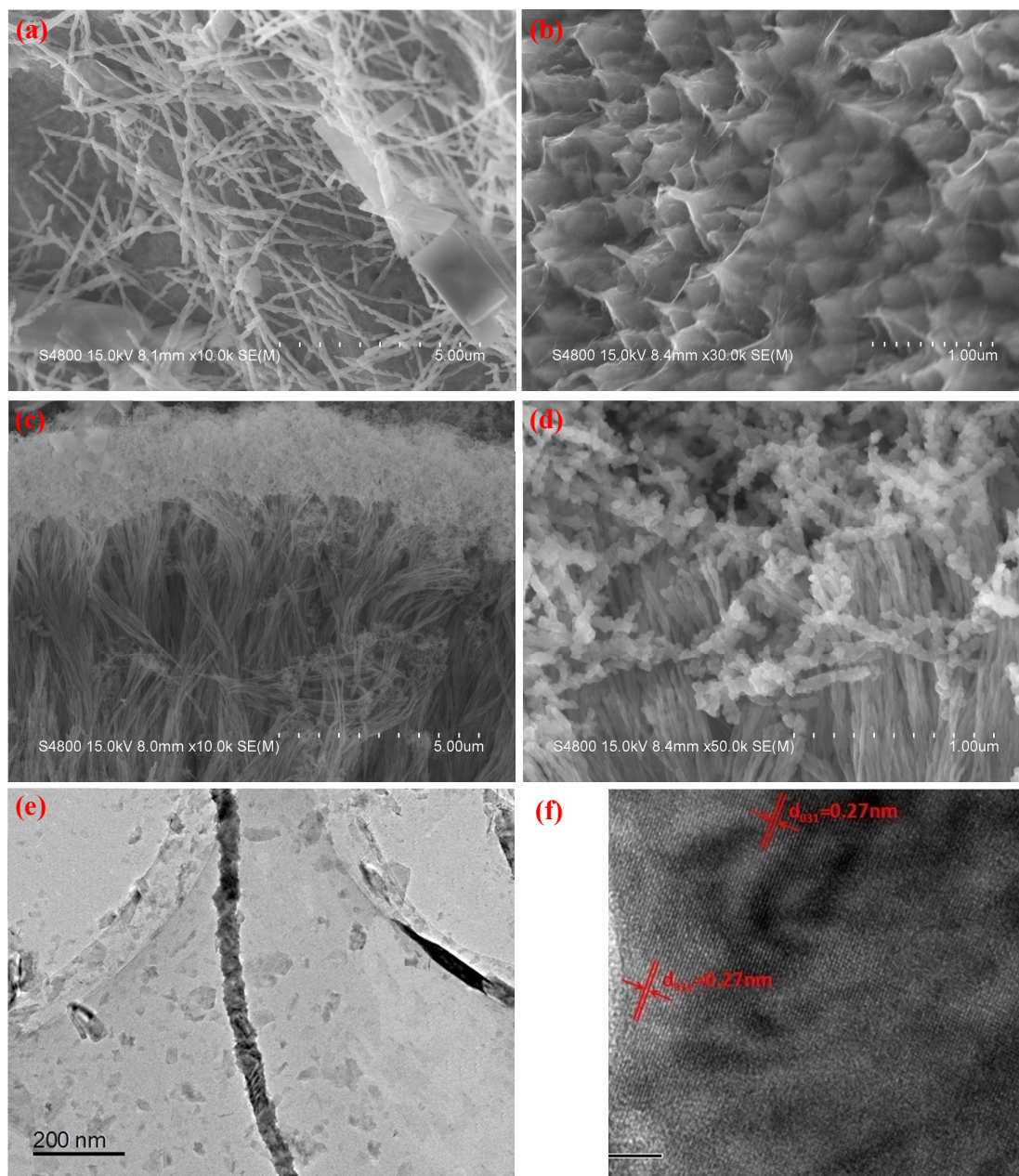


Fig. 2

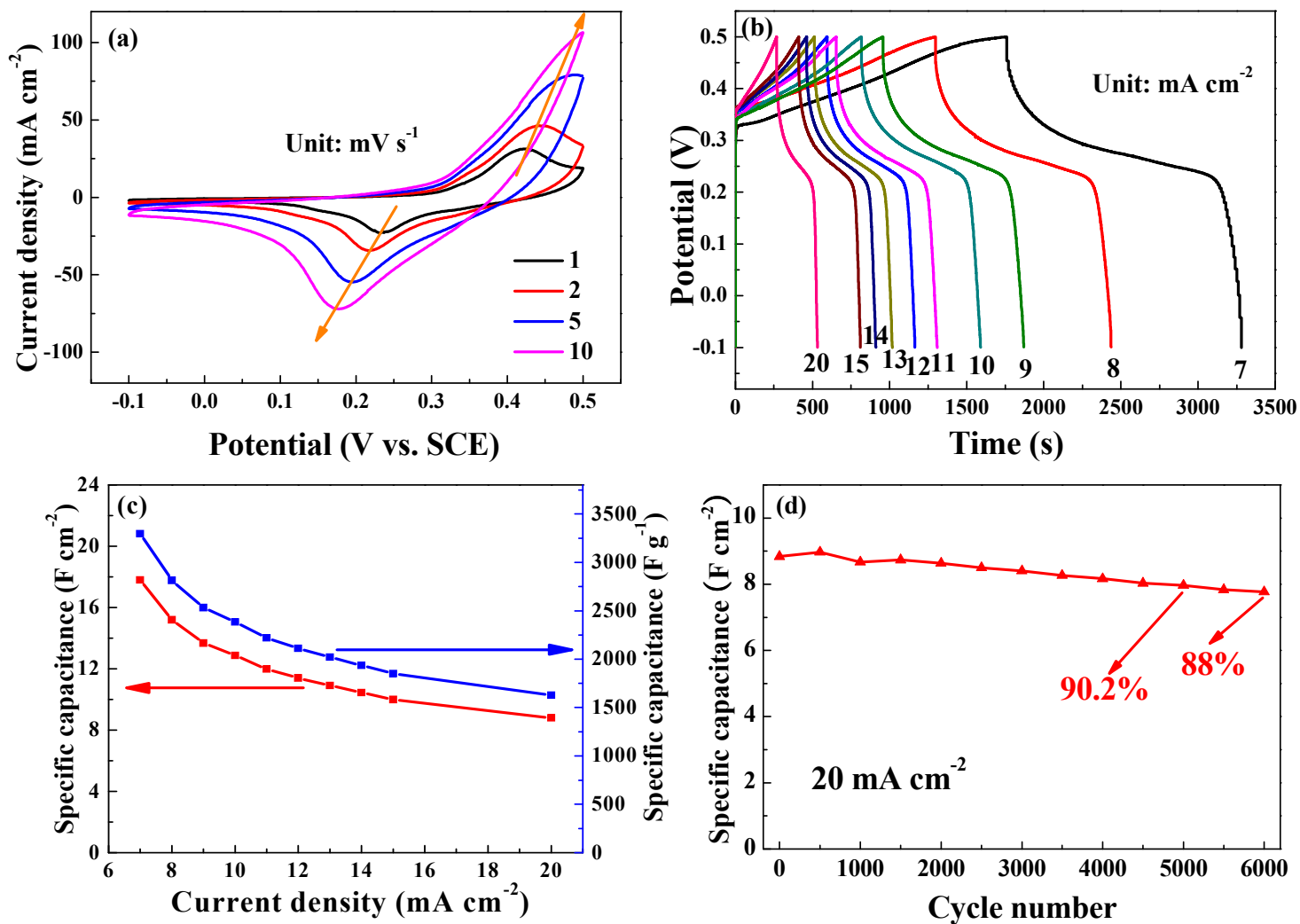


Fig. 3